Applied Optics

Letters to the Editor

One-dimensional Mellin transformation using a single optical element

Robert J. Marks II and John N. Larson

University of Washington, Department of Electrical Engineering, Seattle, Washington 98195.

Techniques for performing 2-D Mellin transforms have been discussed and implemented by Casasent and Psaltis.[1] After the procedure outlined in Refs. 2 and 3, Kellman and Goodman[4] have demonstrated a coherent processor for performing 1-D Mellin transforms. In this letter, we present a method of performing 1-D Mellin transformation which requires only an input placed adjacent a mask and an output plane. The Mellin transformer presented herein is a specific application of the 1-D coherent processors presented in Ref. 5.

The Mellin transform $g(x)$ of a signal $u(\xi)$ is defined as[1,2]

$$g(x) = \int_0^\infty u(\xi) \left(\frac{\xi}{\xi_0}\right)^{j2\pi(x/x_0)-1} d\xi,$$

where the spatial constants, ξ_0 and x_0, are scaling factors included for dimensional consistency. Mellin transformation can be viewed as a linear space-variant operation with line-spread function:

$$h(x;\xi) = \left(\frac{\xi}{\xi_0}\right)^{j2\pi(x/x_0)-1} \mu(\xi),$$

where $\mu(\cdot)$ denotes the unit step function. The processor in Fig. 1 is capable of performing generalized 1-D linear space-variant operations.[5] The relation of the T-mask amplitude transmittance in plane $P1$ to the corresponding line-spread function is[5]

$$T(f_x;\xi) = \exp\left\{\frac{-j\pi}{\lambda f}[x^2 + (\lambda f f_x)^2]\right\} \int_{-\infty}^\infty h(x;\xi) \exp(j2\pi f_x)dx.$$

(1)

$$= \exp\left\{\frac{-j\pi}{\lambda f}[x^2 + (\lambda f f_x)^2]\right\} \delta\left[f_x + \frac{1}{x_0}\ln\frac{\xi}{\xi_0}\right]\left(\frac{\xi_0}{\xi}\right)\mu(\xi),$$

where $\delta(\cdot)$ denotes the Dirac delta, f is the input-output plane separation, and λ is the wavelength of the spatially coherent illumination. The spatial frequency f_x is measured by dividing the vertical displacement in plane $P2$ by λf.

The exponential term in Eq. (1) is recognized as the transmittance of a positive lens of focal length f.[6] The Dirac delta term is approximated by a thin slit bent along the curve

$$f_x = \frac{1}{x_0}\ln\left(\frac{\xi}{\xi_0}\right)\mu(\xi).$$

The (ξ_0/ξ) term is somewhat more troublesome to implement. As is done in Ref. 5, however, we can omit it from the mask and
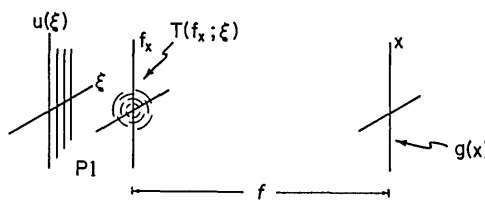

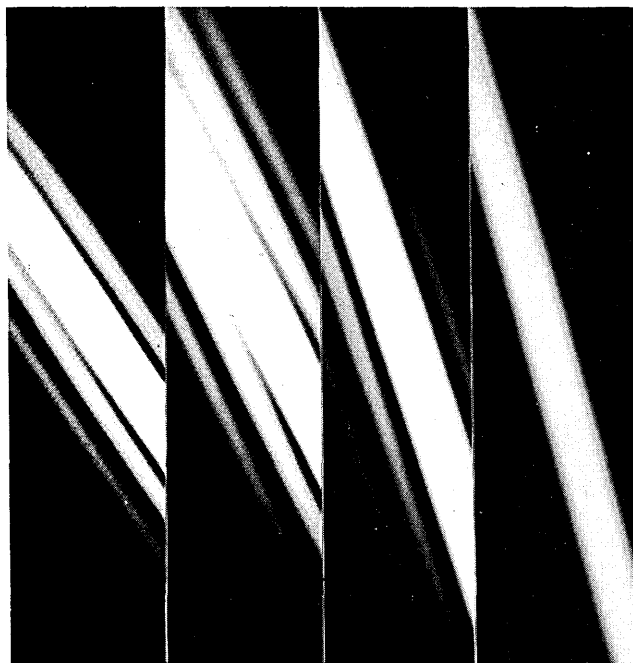Fig. 1. The single optical element coherent processor for performing 1-D Mellin transformation.

Fig. 2. Processor outputs for various unit pulse inputs. The Mellin transform appears along the vertical axis in each case.

recognize that the processor will display the Mellin transform of $(\xi/\xi_0)u(\xi)$ [rather than $u(\xi)$] along the x axis of the plane $P2$.

To investigate the performance of the coherent processor, Mellin transforms were performed on unit amplitude pulses over the interval $a \le \xi \le b$. The resulting Mellin transform is a sinc type function with frequency $\ln b/a$.[1] Keeping the lower limit a constant and decreasing b give the outputs shown in Fig. 2 (left-to-right).
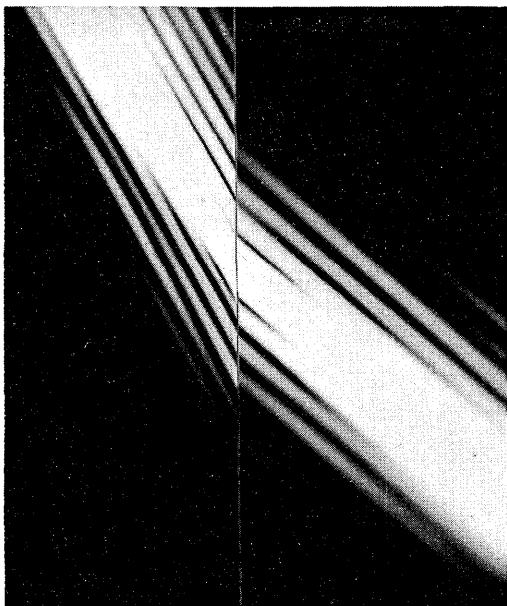
Fig. 3. Processor outputs for two unit pulses differing only in scale. The excellent alignment of these outputs along the vertical axis demonstrates the scale invariance of Mellin transformation.

To illustrate the input scale invariance of the Mellin transform,[1] two separate pulses with common endpoint ratios b/a were input into the processor. As can be seen in Fig. 3, the resulting vertical axis profiles of the processor output are well aligned. This is the desired result.

We have presented a coherent optical processor capable of performing 1-D Mellin transformation with a single optical element. This processor is less efficient in the utilization of incident light than Kellman and Goodman's processor.[4] It does, however, have the advantages of simplicity of implementation, real-space compactness, and total elimination of vignetting.

References

1. J. D. Casasent and D. Psaltis, Proc. IEEE 65, 77 (1977).
2. J. W. Goodman, P. Kellman, and E. W. Hansen, Appl. Opt. 16, 733 (1977).
3. R. J. Marks II, J. F. Walkup, M. O. Hagler, and T. F. Krile, Appl. Opt. 16, 739 (1977).
4. P. Kellman and J. W. Goodman, Appl. Opt. 16, 2609 (1977).
5. R. J. Marks II, M. I. Jones, E. L. Kral, and J. F. Walkup, "One-Dimensional Linear Coherent Processing Using A Single Optical Element," submitted to Applied Optics. 18, 0000 (1979).
6. J. W. Goodman, Introduction to Fourier Optics (McGraw-Hill, New York, 1968).

Far-field speckle and Doppler shifts for rough laser-illuminated rotating cylinders

J. Lynn Smith

U.S. Army Missile Research & Development Command, Research Directorate, Technology Laboratory, Redstone Arsenal, Alabama 35809.

The effect of movement of a rough coherently illuminated body on speckle characteristics has been investigated both experimentally and theoretically.[1-4] Of interest to laser radar applications is the far-field backscatter from rotating objects. George[3] developed a theory describing statistics of speckle in terms of cross-correlations of two field detector outputs, each tuned for one of two frequencies of light illuminating a rotating body. The theory also considers rotational decorrelation and spectral broadening. The last consideration acknowledges the Doppler effect, whereas, in the speckle statistics, rotation rates are assumed negligible.

The question therefore arises: under what conditions can the Doppler effect be ignored when describing the far-field speckle pattern? Obviously, even for a slowly rotating body, the slight shift in wave number multiplied by the often great distance to the observer can change the phase by many radians.

In this Letter simple criteria are derived (for a rough rotating cylinder) to indicate when the Doppler effect is negligible. The physical insight provided can be applied to more complex shapes. We assume the Doppler-induced phase changes are noticeable only over distances large compared with the cylinder.

The electric field at the surface of the cylinder is given by

$$a_2(l,\theta,\theta - \alpha) \approx a(l,\theta,\theta - \alpha) \exp[j\phi(\theta,\theta - \alpha,l)] \exp(jk\Delta r), \quad (1)$$

where

$$\Delta r = \rho - \rho \cos\theta, \quad (2)$$

$$a(l,\theta,\theta - \alpha) = a_0 p_r(l,\theta,\theta - \alpha), \quad (3)$$

in which a_0 is a scalar representing the incident electric field amplitude, and $p_r(l,\theta,\theta - \alpha)$ is the position-dependent surface reflectivity (see Fig. 1). The symbol ϕ represents a phase change of light upon reflection due to roughness at length-position l and angular-position θ for surface orientation α. For small values of θ, $\phi \approx -2kh$, where h is the deviation of the surface from strictly cylindrical. For larger values of θ, ϕ depends on θ. The reflectivity p_r is assumed to vary slowly compared with ϕ so that the two values are essentially independent.
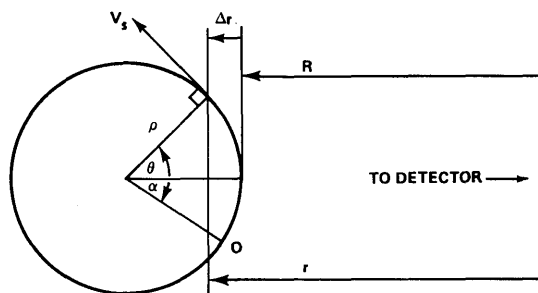

Fig. 1. Geometry for illuminated cylinder.

The Rayleigh-Sommerfield diffraction theory[5] gives the far-field backscatter amplitude for a surface element ds as

$$dA(l,\theta,\theta-\alpha) = \frac{1}{j\lambda} a_2(l,\theta,\theta-\alpha)\frac{1}{r}\exp(jk'r)\cos\theta\, ds, \quad (4)$$

where

$$k' = k \qquad (1 - v_s/c) = k(1 - \rho\omega\sin\theta/c) \quad (5)$$

is the Doppler-modified wave vector. The symbols ω and c represent the angular velocity and speed of light, respectively. Combining eqs. (1) and (4) gives

$$dA = \frac{1}{j\lambda} a\exp(j\phi)\exp(jk\Delta r)\frac{1}{r}\exp(jk'r)\cos\theta\, ds. \quad (6)$$

Since $r = R + \Delta r$ ($\Delta r \ll R$) and, for reasonable values of ω, $k'\Delta r$ may be replaced by $k\Delta r$, then

$$dA \simeq \frac{1}{j\lambda R} a\exp(j\phi)\exp[j(2k\Delta r + k'R)]\cos\theta\, ds, \quad (7)$$

or

$$dA \simeq \frac{1}{j\lambda R}\exp(jkR)a\exp(j\phi)$$
$$\times \exp\left\{jk\left[2\rho(1-\cos\theta)+\left(\frac{k'}{k}-1\right)R\right]\right\}\cos\theta\, ds. \quad (8)$$

Defining the shape factor

$$F(\theta,\gamma) \equiv \exp\{jk[2\rho(1-\cos\theta)-\gamma]\}\cos\theta, \quad (9)$$

where

$$\gamma = R(1 - k'/k) = \rho\omega R\sin\theta/c, \quad (10)$$

the backscattered field amplitude at the detector is

$$A(\alpha,\omega) = \frac{\rho}{j\lambda R}\exp(jkR)\int_0^L\int_{-\pi/2}^{\pi/2} a\exp(j\phi)F(\theta,\gamma)d\theta\, dl. \quad (11)$$

To be rigorous, it should be mentioned that F does not contain all the effect of shape. The roughness phase ϕ and p_r also depend to some extent on shape. However, $F(\theta,\gamma)$ is the factor that contains the Doppler effect.

The term $k\gamma$ in the argument of Eq. (9) represents a displacement in phase which affects the speckle field. However, the effect is only that of a minor change in shape if $0 < \gamma \ll \rho$, or

$$0 \leq \omega R/c \ll 1. \quad (12)$$

Thus the statistics of the backscatter speckle field would be essentially unaffected.

There is a more stringent condition for which even the instantaneous speckle pattern is essentially unaffected, except for apparent angular displacement. Proof follows: The phase in Eq. (9) can be written as $(2k\rho)(1 - \cos\theta - \gamma/2\rho)$. Since $\gamma/2\rho = \omega R\sin\theta/2c \ll 1$, the second factor in this phase is very nearly $1 - \cos\theta\cos(\omega R/2c) - \sin\theta\sin(\omega R/2c)$. Furthermore, the phase term in Eq. (9) may be replaced by $(2k\rho)[1 - \cos(\theta - \omega R/2c)]$ if $2k\rho$ multiplied by the approximation error of the second factor is much less than unity. After expanding sine and cosine functions in the difference between the second factor and its approximation, the condition for replacement becomes $k\rho(\omega R/2c)^2 \ll 1$, or

$$0 \leq \frac{2\pi}{4}\frac{\rho}{\lambda}\left(\frac{\omega R}{c}\right)^2 \ll 1. \quad (13)$$

Thus, in this case,

$$F(\theta,\gamma) \approx \exp\left\{j2k\rho\left[1 - \cos\left(\theta - \frac{\omega R}{2c}\right)\right]\right\} = F\left(\theta - \frac{\gamma}{2\rho\sin\theta}, 0\right). \quad (14)$$

Let $\gamma/[2\rho\sin\theta] = \omega R/2c \equiv \Delta\alpha$, a small angular increment. Noting that $p(l,\theta,\theta-\alpha)$, $\phi(l,\theta,\theta-\alpha)$, and $\cos\theta$ vary slowly with θ (although perhaps rapidly with $\theta - \alpha$), the integrand of Eq. (11) is very nearly

$$a_0 p(l,\theta-\Delta\alpha,\theta-\alpha)\exp[j\phi(l,\theta-\Delta\alpha,\theta-\alpha)]F(\theta-\Delta\alpha,0)$$
$$= a_0 p(l,\theta',\theta'-\alpha+\Delta\alpha)\exp[j\phi(l,\theta',\theta'-\alpha+\Delta\alpha)]F(\theta',0), \quad (15)$$

where $\theta' \equiv \theta - \Delta\alpha$. Since F approaches zero near $\theta = \pm\pi/2$, the integral limits of Eq. (11) may be changed to $\theta' = \pm\pi/2$ without significant effect on the integral. Thus

$$A(\alpha,\omega) \approx C\int_0^L\int_{-\pi/2}^{\pi/2} a_0 p(l,\theta'-\alpha+\Delta\alpha)$$
$$\times\exp[j\phi(l,\theta',\theta'-\alpha+\Delta\alpha)]F(\theta',0)d\theta\, dl$$
$$= A(\alpha - \Delta\alpha, 0), \quad (16)$$

where $C = \rho/(j\lambda R)\exp(jkR)$. More explicitly,

$$A(\alpha,\omega) \approx A\left(\alpha - \frac{\omega R}{2c}, 0\right), \quad \text{Q.E.D.} \quad (17)$$

To summarize, (1) whenever the transverse velocity of the backscatter speckle field at the detector is much less than the speed of light [see inequality (12)], the effect on speckle statistics is slight because the rotating object appears to have only minor shape distortion. The Doppler-induced frequency spread is, of course, still detectable. (2) If the square of the ratio (transverse speckle velocity/c) multiplied by the number of wavelengths in the object radius is much less than unity [see Inequality (13)], any one-look sample of the speckle field is practically unaltered (as well as its statistics). There will be a small apparent angular displacement, however, in addition to the rotation during the transit time R/c. Consider the example for a rough cylinder with $\omega = 2\pi$ rad sec^{-1}, $R = 500$ km, $\lambda = 10^{-6}$ m, and $\rho = 1$ m. Note that $\omega R/c = 1.05 \times 10^{-2}$, which is much less than unity. Thus the speckle statistics, i.e., average intensity and contrast, are not significantly altered. However, since $(\omega R/c)^2\rho/\lambda \approx 10^2$, which is greater than unity, any one-look speckle sample is altered in addition to the small angular displacement.

References

1. A. W. Lohman and G. P. Weigelt, Opt. Commun. 14, 252 (1975).
2. A. W. Lohman and G. P. Weigelt, J. Opt. Soc. Am. 66, 1271 (1976).
3. N. George, J. Opt. Soc. Am. 66, 1183 (1976).
4. J. C. Erdmann and R. I. Gellert, J. Opt. Soc. Am. 66, 1195 (1976).
5. J. W. Goodman, Introduction to Fourier Optics (McGraw-Hill, New York, 1968), pp. 42–45.

Mode elimination in fiber loss measurements

F. T. Stone and P. H. Krawarik

F. T. Stone is with Bell Laboratories, Norcross, Georgia 30071, and P. H. Krawarik is with Western Electric, Engineering Research Laboratories, Princeton, New Jersey 08540.

In an optical fiber the complex interaction of mode dependent loss and mode coupling eventually leads to some steady-state (uniform with length) distribution of power

among the propagating modes of the fiber. To make a measurement that will adequately characterize the behavior of the optical fiber under normal operating conditions, it is important that the mode set launched resemble this steady-state distribution. Otherwise the processes that are going on in the regions of the fiber near the launch point will not be typical of the fiber as a whole. In particular, the launching of cladding modes, leaky modes, and extremely lossy higher order propagating modes (marginal bound modes) must be minimized. There are several approaches to solving this problem, for example, (1) the excitation conditions, i.e., the beam spot size, energy distribution, and divergence (N.A.) can be carefully controlled.[1] This is a deterministic approach that must be applied individually to each fiber. As such it is a lengthy process. (2) A single set of (nominal) excitation conditions can be used for a given class of fibers together with mode strippers (sometimes called mode eliminators or filters) that not only remove the energy in the cladding modes but also eliminate leaky modes and highly lossy (marginal) higher order bound modes. This latter procedure would allow the standardization of measurement conditions. In this Letter we concentrate on the usefulness of mode eliminators in obtaining meaningful loss measurements.

There are several mode stripper designs that have been used in an attempt to remove unwanted power from the fiber before measurement. Among these are: (1) Passing the fiber over black paper, black felt, or a similar material that is saturated with a fluid with refractive index somewhat above that of the cladding. The fiber may or may not be bent or pressed down into the mode stripper material. If the fiber is kept straight in its passage through the mode stripper, only the cladding modes will be affected. (2) Threading the fiber through an S-shaped channel of appropriate dimensions filled with index fluid. To eliminate coating effects the fiber can be stripped of its coating material in its passage through the mode stripper. Arrangements in which the fiber is bent around a linear array of pegs[2] should give results similar to the S-shaped mode stripper. Passing the fiber through a grating mode scrambler, i.e., through opposing sets of teeth that impress microbends of properly chosen period,[3] is another method that has been used to approach steady-state conditions on a fiber quickly.

Our measurements indicate that S-shaped or multiple curvature mode strippers are particularly effective in eliminating power launched into unusually lossy modes. Specifically, we have used a calorimeter[4,5] to measure the loss vs beam position on the fiber face[6-9] of several fibers using different mode stripping techniques. The fibers were manufactured to have a parabolic core profile with a maximum N.A. of 0.23, a core diameter of 55 μm, and a cladding diameter of 110 μm. The experimental arrangement is shown in Fig. 1. Different sets of modes were launched by focusing (using a 10× microscope objective) an unexpanded 633-nm laser beam onto the fiber end face at various values of the core radius. This produced a beam spot diameter of approximately 7 μm with an N.A. of 0.06 (measured at the $1/e^2$ power points). For beam and fiber axes parallel, this excites a group of modes centered about a mode with principal mode number m given by $m/M = (r/a)^2$, where M is the total number of bound modes and a is the fiber core radius.[7] A short (~0.5-m) and a long (~100-m) segment of fiber were used between the mode stripper and the calorimeter to compare the loss immediately after launch with the loss 100 m down the fiber. Several S-shaped mode stripper designs were tried with results similar to those shown in Figs. 2 and 3. The data reported here are for a design found effective for the class of fibers being measured: three regular semicircular grooves of 2.5-cm radius
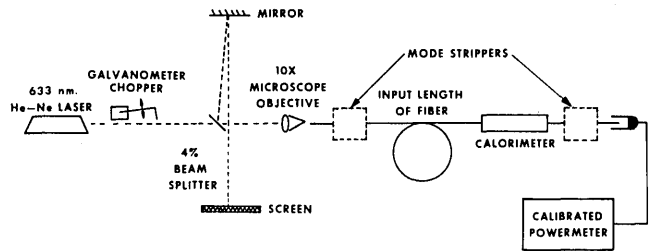

Fig. 1. Experimental arrangement used to measure the effect of different mode strippers. The input length of fiber was either 0.5 m or 100 m.
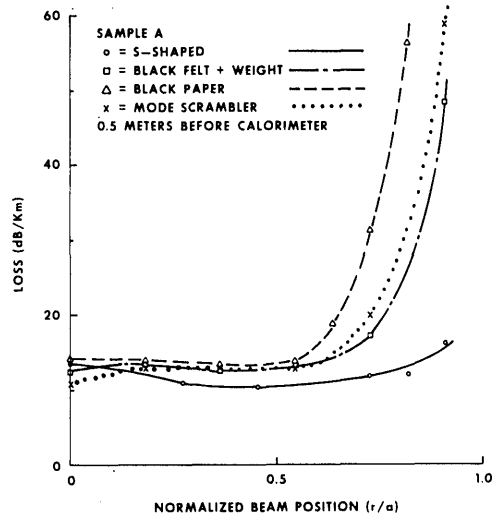
Fig. 2. Fiber loss 0.5 m after launching vs normalized position of low N.A. laser excitation.
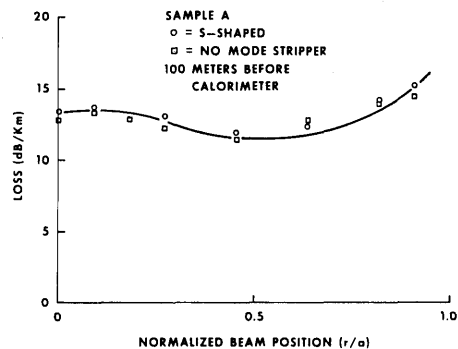
Fig. 3. Same as Fig. 2 but 100 m after launch.

connected to form a serpentine channel that was filled with $n_d = 1.47$ index fluid and through which the uncoated silica-clad fiber was threaded.

Measurements were taken on several fibers with a range of loss values. Those reported below were for a sample with a 633-nm loss of 12.6 dB/km and 820-nm loss of 5.3 dB/km. The results are as follows: (1) For a short length of fiber preceding the calorimeter, the effect of the different mode strippers was pronounced. As shown in Fig. 2, the S-shaped mode strippers were consistently effective in eliminating extremely lossy higher order modes. The others passed varying

amounts of power in such modes as evidenced by the substantially higher loss following the strippers when the fiber was excited near the core–cladding boundary. Carefully pressing the fiber into black felt using a reasonably heavy weight was not so good as using the S-shaped mode stripper; in addition, the exact amount of mode elimination achieved was not completely reproducible. The grating mode scrambler performs its function of spreading the propagating energy out into a broad range of modes quite efficiently. However, for the case where substantial energy is already in the higher order modes, the measurements indicate that the mode scrambler couples more of this energy into unusually lossy modes. (2) When a long length of fiber precedes the calorimeter, the type of mode stripper used makes little difference. Shown in Fig. 3 are plots of the loss vs r/a value for the extreme cases where no mode stripper was used and where the efficient S-shaped mode stripper was used. A comparison of Figs. 2 and 3 reveals that the short length loss results using an S-shaped mode stripper are similar to the long length results using any mode stripper. It should be noted that the 100-m length of input fiber used to obtain the results reported was coated fiber (uv-cured polymer) wound under nonzero tension on a plastic spool. As such it has a certain amount of added microbending loss that preferentially attenuates higher order modes. Such a length was usually sufficient to filter out the unusually lossy modes. In cases where care was exerted to minimize microbending loss (use extremely low loss fiber unwound in a large container), longer lengths were necessary. The point is, however, that the S-shaped mode strippers eliminate the unusually lossy modes immediately.

One thing should be made clear; the S-shaped mode strippers themselves do not establish a steady-state power distribution. When designed as indicated before, they provide little mode mixing (as shown in near-field pattern measurements) and affect only cladding, leaky, and higher order bound modes. Their function is to eliminate these unusually lossy modes that are launched whenever there is power incident near the core–cladding boundary and that are never present in the steady-state modal distribution. Hence in combination with a set of (nominal) excitation conditions that launches a power distribution approximating the steady state, the S-shaped mode stripper can aid in approaching steady-state conditions on a fiber quickly. Loss measurements taken with several test sets adjusted to launch a power distribution approximating the steady state (for example, by matching the short length and long length far field radiation patterns) were lower by anywhere from a few tenths of a dB/km to over 1 dB/km (at 0.82 μm) when the S-shaped mode stripper was used compared with results when the other mode-stripping methods were used. The lower figures agreed well with those measured using the procedure in which the excitation conditions are carefully chosen for each individual fiber [i.e., procedure (1) mentioned at the beginning of this Letter]. It should also be understood that subtle effects may occur over several kilometers of fiber that were not found from these experiments and that larger effects may occur when measuring extremely lossy fiber with very strong differential mode attenuation, i.e., the S-shaped mode stripper does not eliminate enough of the unusually lossy modes to yield a highly accurate loss figure. This latter group of fibers will probably be difficult to measure by any technique and will have either a sharply reduced or peculiarly shaped acceptance angle profile.

In making measurements characterizing optical fibers, for example, a two-point loss measurement, initially it appears a good idea to use a long length of the fiber itself as an input mode filter. This would provide a more uniform with length

(i.e., steady-state) power distribution in the fiber being characterized. This wastes valuable fiber, however, since this reference piece would be cut off and probably discarded. It is possible to use the same long piece of input fiber for all measurements taken, i.e., a single length of fiber that is typical of the fibers being measured. In this case, however, one must be aware not only of uncertainties due to imperfect splices but also of the added loss (i.e., the launching via the splice of excessively lossy modes) due to inherent parameter mismatch resulting from the manufacturing process.[10] Hence it is convenient to bring about an approximation of the uniform power distribution as quickly as possible. Proper adjustment of all excitation variables for each fiber measured can theoretically accomplish this at the cost of increased measurement time. As an alternative, a reasonable one-time-only adjustment of launch conditions based on a typical (nominal) fiber can be made together with the use of efficient mode strippers to eliminate many unusually lossy cladding, leaky, and marginal bound modes. The measurements presented here indicate that S-shaped or multiple curvature mode strippers filled with index-matching fluid are effective in performing this function.

References

1. P. Kaiser, "Numerical-Aperture Dependent Spectral-Loss Measurements of Optical Fibers," in *Proceedings of the International Conference on Integrated Optics and Optical Fiber Communication, Tokyo* (1977), paper B6-2.
2. M. Tokuda, S. Sikai, K. Yochida, and N. Uchida, Electron. Lett. **13**, 146 (1977).
3. G. Zeidler, in *Proceedings 2nd European Conference on Optical Communications,* Paris, France (1976), p. 105.
4. R. L. Cohen, K. W. West, P. D. Lazay, and J. Simpson, Appl. Opt. **13**, 2522 (1974).
5. F. T. Stone, W. B. Gardner, and C. R. Lovelace, Opt. Lett. **2**, 48 (1978).
6. L. Jeunhomme and J. P. Pocholle, Appl. Opt. **17**, 463 (1978).
7. R. Olshansky and S. M. Oaks, Appl. Opt. **17**, 1830 (1978).
8. T. Yamada, H. Hashimoto, K. Inada, and S. Tanaka, "Launching Dependence of Transmission Losses of Graded-Index Optical Fiber," in *Proceedings of the International Conference on Integrated Optics and Optical Fiber Communication, Tokyo,* (1977), paper B6-1.
9. F. T. Stone, Appl. Opt. **17**, 2825 (1978).
10. C. M. Miller, "Effects of Fiber Manufacturing Variations on Graded Index Fiber Splices," in *Proceedings 4th European Conference on Optical Communications,* Genoa, Italy (1978), p. 290.

Spectral radiant exitance of a nonisothermal cavity radiator

James M. Palmer

University of Arizona, Optical Sciences Center, Tucson, Arizona 85721.

The spectral radiant exitance of a blackbody or Planckian radiator can be characterized by a single number, its absolute temperature. Blackbody radiation simulators depart from theoretical blackbodies in one or more of several ways: (1) they have less than unity emittance (due to geometry and/or surface material); (2) they are spectrally selective (nongray); (3) they are non-Lambertian; (4) they are nonisothermal. In

case (1), the spectral radiant exitance can be fully characterized by two numbers, a temperature and an emittance. We use the definition of emittance as the ratio of exitance to that from a Planckian radiator, reserving the word emissivity for a characteristic of a pure material. In cases (2) and (3), a single temperature along with a table, curve, or equation of emittance as a function of wavelength or angle will generally suffice for all but the most accurate work. This assumes that the emittance variation is independent of temperature. If, however, a blackbody radiation simulator is not isothermal (case 4), no combination of a single temperature and a chart, table, or equation of emittance can predict the spectral radiant exitance at other than a single nominal temperature. The radiation must be characterized as a superposition of several blackbody radiators, each modified to account for the spectral surface characteristics and the geometrical factors.

To first demonstrate this fact, the following simple numerical method was used:

(1) Take two, equal, black ($\epsilon = 1$) areas, one with a positive ΔT from some average temperature and the other with an equal but negative ΔT from the same temperature (e.g., $\overline{T} = 500$ K, $\Delta T = 10$ K, therefore $T_1 = 490$ K, $T_2 = 510$ K).

(2) Calculate the total radiant exitance from each area using the Stefan-Boltzmann law (σT^4) and sum to get the total radiant exitance of the composite surface.

(3) Find a single temperature T_c corresponding to the total radiant exitance calculated in step (2).

(4) Find the total radiant exitance for a blackbody at $\overline{T}$.

(5) Calculate the spectral radiant exitance for each of the two temperatures $\overline{T}$ and T_c and for the sum of the spectral radiant exitances for T_1 and T_2.

This procedure was carried out with the aid of a Tektronix 4051 calculator, and the results for one series of calculations are shown in Table I. Using a ΔT of 10 K and an average temperature of 500 K, the total radiant exitance error is small, less than 0.5%. The errors incurred in the spectral radiant exitance are strongly dependent upon wavelength. The plot shown in Fig. 1 has λ/λ_m on the abscissa and the percent error incurred upon assuming that T is correct on the ordinate. Note that the errors for large λT are also quite small, but the errors for small λT become significant. Fortunately for most applications, blackbody radiation simulators are not often used at wavelengths shorter than $\lambda/\lambda_m = 0.4$; therefore, the errors incurred are generally less than 10% if $\Delta T < 2$ K.

A more analytical approach yields essentially the same conclusions. If we start with the Planck equation,

$$M_\lambda = \frac{c_1}{\lambda^5} [\exp(c_2/\lambda T) - 1]^{-1}, \qquad (1)$$

and let $c_2/\lambda T$ be denoted as x, then

$$M_{\lambda 1} = \frac{c_1}{\lambda^5} [\exp(x_1) - 1]^{-1}, \qquad (2a)$$

$$M_{\lambda 2} = \frac{c_1}{\lambda^5} [\exp(x_2) - 1]^{-1}, \qquad (2b)$$

for the two equal areas. Let the sum of the spectral radiant exitances be $M_{\lambda T}$. Then

$$M_{\lambda T} = M_{\lambda 1} + M_{\lambda 2}, \qquad (3)$$

and this reduces to

$$M_\lambda T = \frac{c_1}{\lambda^5} \left[\frac{\exp(x_1) + \exp(x_2) - 2}{\exp(x_1 + x_2) - \exp(x_1) - \exp(x_2) + 1} \right]. \qquad (4)$$

Now set this exitance equal to that from another blackbody with twice the area at temperature T_c:

Table I. Spectral and Total Radiant Exitances of a Blackbody Radiation Simulator with Two Isothermal Zones, $T_1 = 490$ K and $T_2 = 510$ K

WL (μm)	$(M1 + M2)/2$	M at T (corr)	M at T (avg)
1	1.3776E-8	1.2114E-8	1.1907E-8
2	6.8315E-4	6.6529E-4	6.5958E-4
3	1.0666E-2	1.0573E-2	1.0513E-2
4	2.7669E-2	2.7582E-2	2.7464E-2
5	3.8196E-2	3.8161E-2	3.8030E-2
6	4.0200E-2	4.0204E-2	4.0088E-2
7	3.7173E-2	3.7196E-2	3.7103E-2
8	3.2217E-2	3.2245E-2	3.2174E-2
9	2.7027E-2	2.7054E-2	2.7001E-2
10	2.2325E-2	2.2349E-2	2.2309E-2
11	1.8331E-2	1.8351E-2	1.8320E-2
12	1.5041E-2	1.5058E-2	1.5035E-2
13	1.2372E-2	1.2386E-2	1.2367E-2
14	1.0218E-2	1.0230E-2	1.0215E-2
15	8.4825E-3	8.4917E-3	8.4803E-3
16	7.0805E-3	7.0880E-3	7.0789E-3
17	5.9439E-3	5.9502E-3	5.9428E-3
18	5.0182E-3	5.0234E-3	5.0174E-3
19	4.2604E-3	4.2647E-3	4.2597E-3
20	3.6365E-3	3.6402E-3	3.6360E-3
SUM	0.32654	0.32651	0.32569

At $T_1 = 490$ K, total radiant exitance $M_1 = 0.3268$ W-cm^{-2}.
At $T_2 = 510$ K, total radiant exitance $M_2 = 0.3836$ W-cm^{-2}.
Average radiant exitance (0.5 ea) = 0.3552 W-cm^{-2}.
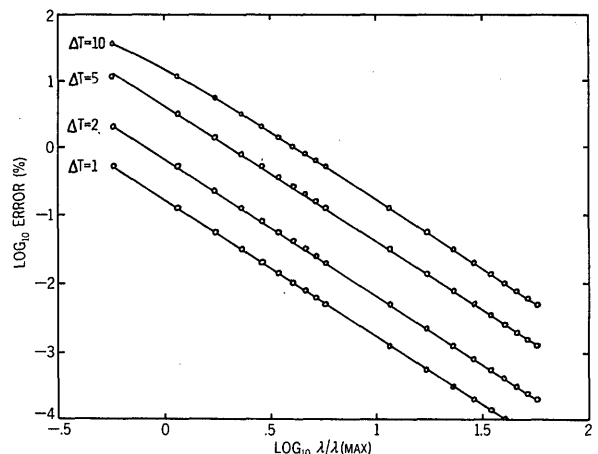Temp. corresponding to 0.3552 W-cm^{-2} = 500.3 K.
Average temperature = 500 K.

Fig. 1. Errors in spectral radiant exitance of a nonisothermal blackbody radiation simulator vs λ and ΔT.

$$\frac{2c_1}{\lambda^5} [\exp(x_c) - 1]^{-1} = \frac{c_1}{\lambda^5} \left[\frac{\exp(x_1) + \exp(x_2) - 2}{\exp(x_1 + x_2) - \exp(x_1) - \exp(x_2) + 1} \right], \qquad (5)$$

and this reduces to

$$\exp(x_c) = \frac{2 \exp(x_1 + x_2) - [\exp(x_1) + \exp(x_2)]}{\exp(x_1) + \exp(x_2) - 2}. \qquad (6)$$

Let $x_2 = x + \Delta x$ and $x_1 = x - \Delta x$ [where $\Delta x = (-c_2/\lambda T^2) \Delta T$], then Eq. (6) becomes

$$\exp(x_c) = \frac{2 \exp(x) - [\exp(\Delta x) + \exp(-\Delta x)]}{[\exp(\Delta x) + \exp(-\Delta x)] - 2 \exp(-x)}. \qquad (7)$$
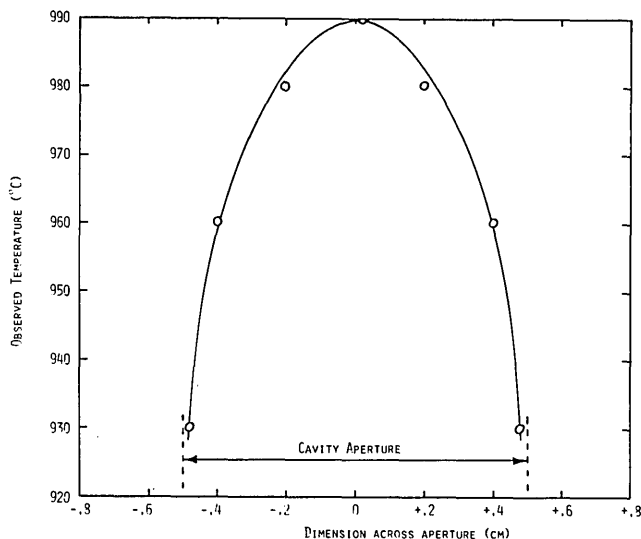
Fig. 2. Variation in temperature observed with optical radiation pyrometer across the aperture of a 23° conical cavity blackbody radiation simulator.

[Note: if Δx is reduced to zero, $\exp(x_c)$ approaches $\exp(x)$ as expected.] The percent error is

$$100\left[1 - \frac{\exp(x_c)}{\exp(x)\cosh(\Delta x)}\right].\qquad(8)$$

This equation was used to calculate the data in Fig. 1.

The impetus for this study arose from the use of a vintage 1960 commercial ir radiation reference source for calibration of an optical pyrometer and an ir thermograph. This unit is factory rated at ±5 K absolute accuracy and has a stated emittance of 0.99 ± 0.01. When operated at its maximum rated temperature of 1000°C, a gradient along the walls was easily seen with the unaided eye. Measurements were made with an optical radiation pyrometer, and the results are shown in Fig. 2, a graph of the temperature as a function of position across the 2.54-cm cavity opening. Note that the hottest area is at the center of the 23° conical cavity and is about 990°C. Near the edge of the aperture, the temperature is about 940°C. The total radiance near the edge is 81.3% of the center radiance. The ratio of spectral radiances from the edge to the center as a function of wavelength is shown in the following:

wavelength (μm)	0.5	1	2	3	5	10
ratio (edge/center)	0.214	0.462	0.679	0.771	0.850	0.905

Several conclusions can be drawn from these results. Foremost is that great pains must be taken to ensure that the blackbody radiation simulator is indeed isothermal under every conceivable working condition. This can be achieved by using a spherical[1] rather than a cylindrical or conical cavity shape, or by other procedures in the cavity designs. If it cannot be made isothermal over its entire surface (for example, if you are stuck with a unit similar to the one described above), make sure that you test the radiance distribution as a function of angle before using it, especially when testing a low $F/\#$ system; then use only the area which is isothermal. If this is not feasible, the only recourse is to measure the temperature distribution and perform the superposition as described above.

I would like to thank W. L. Wolfe and F. O. Bartell for their helpful discussions.

Reference

1. F. O. Bartell and W. L. Wolfe, Infrared Phys. 16, 13 (1976).

Quantum efficiency of the *p-n* junction in silicon as an absolute radiometric standard

Jon Geist

National Bureau of Standards, Washington, D.C. 20234.

The most widely used detector of optical radiation is the silicon photodiode. The physics of this device is well understood, and its technology is quite advanced. It is based on the *p-n* junction in silicon, which has been the subject of intense and thorough study because of its widespread application in solid state electronics and solar cells.

When a silicon photodiode is used to measure optical radiation in absolute units, its calibration is not based on the physics of silicon. Instead the calibration is based on the thermal physics of either blackbody radiators[1] or electrical substitution radiometers.[2] The highest accuracy currently demonstrated for either of these techniques is on the order of one-tenth of 1%,[3] and it was achieved only with considerable difficulty. The accuracies achieved in more routine calibrations do not approach this level.[4,5] For this reason, and because silicon technology is so highly advanced, it has been suggested that calibrations of comparable or even higher accuracy could be obtained directly from the electrical and/or optical characteristics of the photodiode itself. In fact, in the red portion of the visible spectrum the sum of the specular reflectance and the external quantum efficiency of shallow junction silicon photovoltaics falls within a few tenths of 1% of unity. Therefore, all that is needed is a physical model that describes the small defect in the internal quantum efficiency of this type of device, and which is in a form suitable for high accuracy applications. The remainder of this Letter will be devoted to this task.

It is convenient to divide the typical silicon photovoltaic detector into four regions: the antireflection coating; the front diffusion region; the bulk region; and the rear diffusion region. The following analysis is restricted to wavelengths for which negligible radiation is absorbed in the antireflection coating. This condition is satisfied throughout the visible and near ir by grown SiO_2 coatings, but not by vacuum deposited coatings of the same material.[6]

Within the front diffusion region, the doping concentration and minority carrier diffusion length vary by many orders of magnitude. The exact nature of these variations is not readily determined, so neither analytic nor numerical solutions of the minority carrier diffusion equation can be used. However, the contribution of this region to the internal quantum efficiency at wavelength λ can be expressed as

$$\epsilon_F = \int_0^F \exp(-\alpha x)\alpha P(x)dx,\qquad(1)$$

where x is the distance into the silicon material, F is the depth of the front diffusion region, α is the spectral absorption coefficient (we have suppressed the functional dependence on λ), and $P(x)$ is the collection efficiency distribution function. In other words $P(x)$ is the probability that an excess

minority carrier generated at position x will cross the junction before recombination.

In the bulk region, the doping concentration and minority carrier diffusion length are both independent of position, and analytic solutions for the contribution of this region to the internal quantum efficiency have been published.[7] The present treatment is further restricted to wavelengths for which negligible radiation is absorbed in the rear diffusion region. Therefore, this region makes no direct contribution to the detector's quantum efficiency. However, it makes an important indirect contribution by repelling the minority carriers away from the rear electrode where recombination would take place.[8]

Two unstated assumptions are implicit in the photovoltaic model that we are using. First, every supra-bandgap photon absorbed in the silicon must result in the creation of exactly one electron–hole pair. Second, the absorption coefficient of the silicon in the front diffusion region must be identical to that in the bulk region and, therefore, independent of doping level. The internal quantum efficiency can now be calculated subject to the assumptions stated above by adding Eq. (1) to the contribution from the base region (see Ref. 7) with the rear surface recombination velocity set equal to zero to describe the effect of the rear diffusion region. The result can be put in the form

$$\epsilon = 1 + \sum_{n=1}^{\infty} (-1)^n \alpha^n \langle x^n \rangle / n!$$
$$+ \exp(-\alpha F) \left[\frac{1}{(\alpha L)^2} - \frac{\tanh(B/L)}{\alpha L} \right.$$
$$\left. - \exp(-\alpha B) \operatorname{sech}(B/L) \right] \left[1 - \frac{1}{(\alpha L)^2} \right]^{-1}, \quad (2)$$

where

$$\langle x^n \rangle = \int_0^F x^n P'(x) dx, \quad (3)$$

and where B is the thickness of the bulk region, L is the minority carrier diffusion length, and the prime in Eq. (3) represents differentiation with respect to x. To obtain Eq. (2) in the form shown, it is necessary to integrate Eq. (1) by parts, to expand the exponential in a Taylor series, and to interchange the order of summation and integration. The quantity $P(F)$ has been set equal to one in Eq. (2). This is a very good approximation because F is chosen such that $P(F)$ is a maximum. This occurs to the rear of, but very near to, the junction, where the lifetime is of the order of 1 msec, and the time required to sweep a minority carrier across the junction is less than 10^{-10} sec.[9,10]

Equation (2) can be used to establish an absolute radiometric scale based only on relative radiometric measurements. Let λ_1, λ_2, and λ_3 be wavelengths in the vicinity of 400 nm, 750 nm, and 950 nm, respectively. For a shallow junction photodiode, the infinite sum in Eq. (2) is accurately approximated by the first term in the sum, and the two ratios $\epsilon(\lambda_1)/\epsilon(\lambda_2)$ and $\epsilon(\lambda_3)/\epsilon(\lambda_2)$ uniquely determine L and $\langle x \rangle$, subject to the assumption that F, B, and the spectral dependence of $\alpha(\lambda)$ are known. An iterative solution is required. Once L and $\langle x \rangle$ are determined, the absolute spectral dependence of $\epsilon(\lambda)$ can be calculated. The key idea is that the ratios $\epsilon(\lambda_1)/\epsilon(\lambda_2)$ and $\epsilon(\lambda_3)/\epsilon(\lambda_2)$ can be determined from relative radiometric measurements, yet through Eq. (2), they establish a scale of the absolute quantity $\epsilon(\lambda)$.

Since the iterative solution procedure and error analysis are somewhat involved, their details are beyond the scope of this paper. The results, however, are quite encouraging. An uncertainty of less than ±0.25% of value is predicted around

750 nm, based on the estimate that Dash and Newman's absorption coefficients are good to ±10% of value and that ±0.2% of value is possible in relative radiometric measurements. The former estimate is based on the agreement between Dash and Newman's[11] data and Philipp's[12] later redetermination, and the latter reflects the author's experience with this type of measurement. Future research should decrease both uncertainties substantially.

The physics behind the proposed procedure will now be reviewed. One plus the infinite sum in Eq. (2) is a generalization of the dead layer model of Lindmayer and Allison.[6,13] It reduces to $\exp(-\alpha t)$ if, and only if, $P'(x)$ is the Dirac delta function, $\delta(x - t)$. This is equivalent to the conventional dead layer model wherein the collection efficiency $P(x)$ is zero for $x < t$, but unity for $x > t$. The advantage of the generalized model is that it allows for arbitrary variations of the collection efficiency distribution in the front diffusion region and is therefore more realistic.

The quantities $\langle x \rangle$, F, B, and L are of the order of 15 nm, 100 nm, 300 μm, and 1 mm, respectively, for shallow junction photodiodes with long minority carrier lifetimes in the bulk region. In this case, the internal quantum efficiency is accurately approximated by the much simpler equation

$$\epsilon \approx y = 1 - \alpha t - B/\alpha L^2, \quad (4)$$

where t has been set equal to $\langle x \rangle$ to establish the relation to the dead layer model.

Table I compares values of ϵ calculated from Eq. (4) with those calculated from Eq. (2) assuming a true dead layer. It can be shown that if $P(x)$ is a nondecreasing function of x in the front diffusion region, $\exp(-\alpha t)$ and $1 - \alpha t$ are, respectively, upper and lower bounds to one plus the infinite sum appearing in Eq. (2), provided that $\alpha t \ll 1$. Therefore, the differences that appear in Table I at the short wavelengths are bounds to the variation arising from different (nondecreasing) functional forms for $P(x)$ in the front diffusion region. Thus, for shallow function photodiodes, the dead layer model is considerably more accurate than might have been expected on the basis of the highly idealized form of $P(x)$ that is the basis of the model. The differences in Table I at the long wavelengths are due to inadequacies in the approximations leading to Eq. (4).

Dash and Newman's data on the absorption coefficient of silicon[11] were used in preparing Table I, and their values are summarized in the table. Notice that the absorption coefficient of silicon decreases by over 2 orders of magnitude from

Table I. Spectral Dependence of Internal Quantum Efficiency of Typical Shallow Junction Silicon Photodiode

Wavelength	Quantum efficiency		Absorption coefficient (μm^{-1})
	Eq. (2) (rigorous)	Eq. (4) (approximate)	
400	0.8991	0.8936	7.09
450	0.9656	0.9649	2.33
500	0.9835	0.9834	1.09
550	0.9888	0.9887	0.723
600	0.9926	0.9925	0.456
650	0.9940	0.9939	0.349
700	0.9954	0.9953	0.225
750	0.9959	0.9957	0.156
800	0.9957	0.9955	0.100
850	0.9945	0.9940	0.0588
900	0.9921	0.9910	0.0356
950	0.9859	0.9851	0.0206

Note: $t = 15$ nm, $F = 100$ nm, $B = 300$ μm, and $L = 1$ mm.

400 nm to 950 nm, and that the third term in Eq. (4) is negligible at short wavelengths, whereas the second term is negligible at long wavelengths. Thus it is reasonable to talk about a short and a long wavelength defect mechanism in the photodiode's internal quantum efficiency. The former is associated with the dead layer and the latter with the bulk region.

Notice also that Eq. (4) has a maximum value of $1 - (2/L)(Bt)^{1/2}$ and that it occurs at the wavelength for which $\alpha = (1/L)(B/t)^{1/2}$. At this wavelength, both mechanisms contribute equally to the defect in the internal quantum efficiency. The same nominal values that were used in computing Table I yield a value of 0.9958 as the maximum value of Eq. (4) and 0.141 μm^{-1} as the value of α for which the maximum occurs. This corresponds to a wavelength around 760 nm. All the above results apply rigorously to Eq. (4) and approximately to Eq. (2).

I acknowledge useful discussions about this topic with A. Russell Schaefer.

References

1. H. J. Kostkowski, D. E. Erminy, and A. T. Hattenburg, Adv. Geophys. 14, 111 (1970).
2. W. R. Blevin and W. J. Brown, Aust. J. Phys. 20, 567 (1967).
3. W. R. Blevin and W. J. Brown, Metrologia 7, 15 (1971).
4. D. B. Betts and E. J. Gillham, Metrologia 4, 101 (1968).
5. M. Suzuki and N. Ooba, Metrologia 12, 123 (1976).
6. J. Lindmayer and J. F. Allison, COMSAT Tech. Rev. 3, 10 (1973).
7. H. J. Hovel, Semiconductors and Semimetals, Vol. 11, Solar Cells (Academic, New York, 1975), pp. 15–20.
8. Ref. 7, p. 23, 24.
9. P. H. Wendland, Proc. Tech. Program, E-O/Laser 77, Anaheim, Calif., 1977 (Industrial and Scientific Conference Management, Chicago, 1977), p. 6.
10. Ref. 6, pp. 9, 10.
11. W. C. Dash and R. Newman, Phys. Rev. 99, 1151 (1955).
12. H. R. Philipp, J. Appl. Phys. 43, 2835 (1972).
13. D. Redfield, Appl. Phys. Lett. 33, 531 (1978).

APPLICATIONS OF SPACE FLIGHT IN MATERIALS SCIENCE AND TECHNOLOGY

by Shirleigh Silverman (deceased) and Elio Passaglia

The proceedings of the April 1977 Conference on the Applications of Space to Materials Science and Technology review the materials science experiments carried out in space and assess the possible future applications of space research in materials science and technology with the advent of the space shuttle. Experiments carried out on Skylab, the Appolo-Soyuz Test Project, and recent sounding rocket experiments are described. Specific discussions directed at possible future applications in metals and alloys, ceramics, semiconductor materials, biological materials, crystal growth, transport properties, critical phenomena, thermodynamic data, containerless processing, combustion, and convection effects are also included.